Article

Protein Sizing with Differential Dynamic Microscopy

Chiara Guidolin, Christopher Heim, Nathan B. P. Adams, Philipp Baaske, Valeria Rondelli, Roberto Cerbino,* and Fabio Giavazzi*

Cite This: *Macromolecules* 2023, 56, 8290−8297

Read Online

ACCESS | Metrics & More | Article Recommendations | Supporting Information

ABSTRACT: Introduced more than 50 years ago, dynamic light scattering (DLS) is routinely used to determine the size distribution of colloidal suspensions as well as of macromolecules in solution, such as proteins, nucleic acids, and their complexes. More recently, differential dynamic microscopy (DDM) has been proposed as a way to perform DLS experiments with a microscope, with much less stringent constraints in terms of cleanliness of the optical surfaces but a potentially lower sensitivity due to the use of camera-based detectors. In this work, we push bright-field DDM beyond known limits and show it to be sufficiently sensitive to size small macromolecules in diluted solutions. By considering solutions of three different proteins (bovine serum albumin, lysozyme, and pepsin), we accurately determine the diffusion coefficient and hydrodynamic radius of both single proteins and small protein aggregates down to concentrations of a few milligrams per milliliter. In addition, we present preliminary results showing an unexplored potential for the determination of virial coefficients. Our results are in excellent agreement with those obtained in parallel with a state-of-the-art commercial DLS setup, showing that DDM represents a valuable alternative for rapid, label-free protein sizing with an optical microscope.
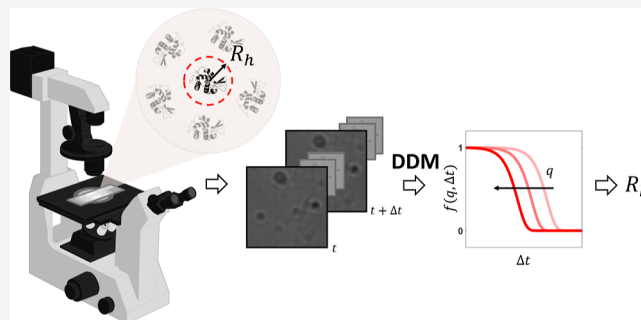
INTRODUCTION

Dynamic light scattering (DLS) is an extremely sensitive optical method to probe the dynamics of complex fluids: coherent light with wavelength λ illuminates the sample, and the temporally fluctuating scattering intensity at an angle θ is quantitatively analyzed to extract the lifetime of the refractive index fluctuations occurring in the sample at the length-scale $L \simeq \lambda/2 \sin(\theta/2)$.[1,2] For a diluted suspension of small particles, the refractive index distribution is mainly determined by the particle concentration, which fluctuates over time due to Brownian motion. In this case, measuring the correlation time of the intensity fluctuations enables estimating the diffusion coefficient of the particles from which, if the viscosity of the solvent is known, their hydrodynamic radius can be determined via the Stokes−Einstein relation.[3] First demonstrated in the late 1960s as a rapid and noninvasive method to measure the size of proteins, nucleic acids, viruses, and synthetic nanoparticles in solution,[4,5] DLS rapidly grew in popularity, and nowadays commercial DLS instruments are part of the standard instrumentation of many pharmacology, physics, biology, and chemistry laboratories, both in academic and in industrial contexts. Since its introduction, one of the key applications of DLS has been the determination of the size of macromolecules and supramolecular structures in a range roughly comprised between a fraction of a nanometer and a few microns.[6] Moreover, the strong dependence of the scattered intensity I on the particle size (for small particles I

scales as the sixth power of the radius[7]) makes DLS particularly effective in detecting the presence of aggregates and monitoring aggregation processes.[6]

A downside of the excellent sensitivity of DLS is its extreme susceptibility to the presence of impurities both in the sample and along the optical path, implying meticulous care in sample preparation (e.g., the need for multiple filtration steps) and high cleanliness standards for all the optical surfaces.[6] Moreover, due to its strong susceptibility to multiple scattering, DLS is suitable for probing only fairly transparent solutions. This strongly narrows the range of concentrations that DLS can probe and prevents its application to even slightly turbid materials or harsh experimental conditions. To overcome these limitations, different variants have been proposed over the years, aimed either at reducing the effect of multiple scattering, for example, exploiting different cross-correlation schemes, as in two-color and three-dimensional DLS,[8] or at extracting dynamical information from the multiple scattered light, as in diffusing wave spectroscopy (DWS).[9] However, except for DWS, which operates in the strong
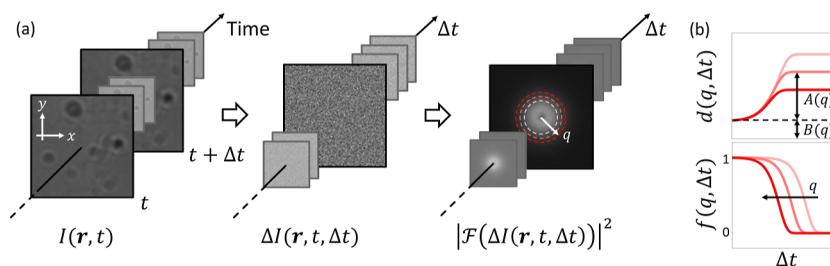
Figure 1. DDM analysis. (a) A sequence of sample images $I(\mathbf{r}, t)$ is recorded with a constant frame rate. Frames at increasing time delays are subtracted from each reference frame to get difference images: $\Delta I(\mathbf{r}, t, \Delta t) = I(\mathbf{r}, t + \Delta t) - I(\mathbf{r}, t)$. The Fourier transform of the image difference, and its squared modulus, is then calculated, $|\mathcal{F}(\Delta I(\mathbf{r}, t, \Delta t))|^2$. The image structure function $d(\mathbf{q}, \Delta t)$ is retrieved by averaging the Fourier power spectra obtained for the same time delay Δt but different reference times t. The system isotropy allows considering the azimuthal average of $d(\mathbf{q}, \Delta t)$. (b) For each wavevector q, the azimuthally averaged image structure function can be plotted against the lag time Δt and can be written as $d(q, \Delta t) = A(q)[1 - f(q, \Delta t)] + B(q)$, where $A(q)$ is the static amplitude, $B(q)$ is the noise term, and $f(q, \Delta t)$ is the real part of the intermediate scattering function.

multiple scattering limit and is suitable for highly turbid materials, none of the aforementioned alternatives to DLS have achieved comparable commercial success, mainly due to the increased operational and instrumental complexity compared to standard DLS.

In 2008, Cerbino and Trappe demonstrated that a conventional optical microscope using white-light illumination could be used to extract the same information obtained with DLS, by analyzing temporal sequences of images of the sample acquired in direct space.[10] This approach, named differential dynamic microscopy (DDM), relies on a fully automated and operator-independent procedure that calculates simultaneously for different wavevectors q the temporal correlations of the spatially Fourier-transformed sample images.[11] DDM has been successfully demonstrated in a wide range of applications including the characterization of the Brownian dynamics of diluted[10,12] and concentrated[13,14] colloidal suspensions, the microrheology of complex fluids,[15−17] the active motion of swimming microorganisms[13,18,19] and crawling cells,[20] the protein absorption on functionalized nanoparticles,[21] and the diffusive behavior of large protein clusters.[22]

The close formal correspondence with DLS enabled expanding the range of applicability of DDM by directly exploiting or adapting both well-established experimental geometries (like depolarized[23,24] or wide-angle scattering[25] to measure the rototranslational dynamics of anisotropic particles) and analytical tools (like cumulant expansions[22,24] to estimate polydispersity or even more refined inversion schemes, like CONTIN,[26] to access the particle size distribution).

The most obvious advantage of DDM is that it does not require any dedicated or specialized instrumentation. Other key strengths, which fostered adoption in an increasing number of laboratories worldwide, include its robustness with respect to the presence of dirt along the optical path,[10] the tolerance with respect to multiple scattering,[27] the possibility of exploiting different imaging modes and optical contrast mechanisms, and even combining them[20,28,29] to gather information on different substructures.

To date, one of the main limitations of bright-field DDM compared to DLS is its sensitivity, namely, the ability to reliably measure very small, weakly scattering particles, a case that includes a variety of interesting biological macromolecules. In this work, we experimentally show that bright-field DDM can successfully probe the dynamics of diluted protein solutions, down to concentrations of a few mg/mL; the

smallest detected macromolecule (lysozyme) has a hydrodynamic radius of about 2 nm, 1 order of magnitude below the previous detection limit,[30] which opens a whole new field of application for this technique.

■ MATERIALS AND METHODS

Sample Preparation and Imaging. In this study, we consider aqueous solutions of three different proteins: bovine serum albumin (BSA) (Sigma #A7638), pepsin (Roche #10108057001), and lysozyme (Roche #10837059001). Phosphate-buffered saline (PBS) was prepared from commercial 10× stock solutions (ROTH #1058.1). For each protein, we probed four different concentrations, obtained by serial dilution. Before measurement, each solution is filtered with 0.22 μm filters (Minisart).

Filtration and possible protein adsorption to the vials can, in principle, alter the actual protein concentration in the sample, which can differ from its nominal value. To account for these effects, a commercial UV spectrophotometer (Thermo Fisher Scientific) was used to independently assess the actual protein concentration within each sample. By measuring the sample absorbance a at a wavelength λ = 280 nm, the protein concentration is then obtained by inverting the Beer−Lambert law, $a = \varepsilon c l$, where ε is the protein extinction coefficient, c is the concentration, and l = 0.1 cm is the optical path length. The concentrations are reported in Supporting Information Table S1, together with the extinction coefficients used for their calculation.

For microscopy measurements, the samples are confined in glass capillaries with rectangular cross sections (thickness 300 μm, and width 3 mm). Each capillary is then put on a microscope slide and carefully sealed with epoxy glue at the two ends to prevent evaporation.

The experimental setup consists of a commercial inverted microscope (Nikon Eclipse Ti−U) equipped with a fast digital camera (Hamamatsu Orca Flash 4.0 v2). Bright-field images of the sample are collected with a 20 × 0.5 NA objective. For each sample, four sequences of 5000 images are recorded with a sampling rate of 500 fps and an exposure time of 1.99 ms. For each solution, image sequences are collected from two distinct portions of the sample, the focal plane corresponding to the middle plane of the capillary. Image resolution is 1024(w) × 128(h) pixels, upon 2 × 2 binning. The effective pixel size, taking into account the lens magnification and binning, is equal to 650 nm. The imaging conditions, in terms of illumination intensity, size of the field diaphragm, and size aperture diaphragm as well as the camera settings, are carefully maintained constant throughout the whole set of experiments. All the experiments are performed at room temperature T = (22 ± 2) °C.

All of the samples are characterized in parallel with a state-of-the-art commercial DLS instrument (Prometheus Panta, NanoTemper Technologies GmbH) with λ = 405 nm and θ = 147° for comparison. Samples were filled into Prometheus High Sensitivity capillaries, and

10 acquisitions were measured per capillary at 6% UV excitation power and 100% DLS power at 25.0 °C using PR.Panta Control v.1.5.2. Additional static light scattering measurements have been performed using a custom-built apparatus equipped with a $\lambda = 532$ nm laser source.[31]

DDM Analysis for Protein Sizing. Protein diffusive dynamics is probed in the reciprocal space according to DDM analysis, whose main steps are schematically illustrated in Figure 1. A detailed description of the technique can be found for example in refs.,[10,11] while a number of software implementations of the method have been made publicly available by different groups in the past few years.[32,33] In short, the procedure is based on the acquisition of a sequence of bright-field microscopy images, $I(\mathbf{r}, t)$ with a constant frame rate. Frames separated by a given time delay Δt are subtracted from each other to generate a difference image, $\Delta I(\mathbf{r}, t, \Delta t) = I(\mathbf{r}, t + \Delta t) - I(\mathbf{r}, t)$, as depicted in Figure 1a. A 2D fast Fourier transform algorithm is then applied to the difference image, and the spatial Fourier power spectra obtained for the same time delay Δt, but different initial times t, are then averaged to get the so-called image structure function $d(\mathbf{q}, \Delta t) \equiv \langle |\mathcal{F}(\Delta I(\mathbf{r}, t, \Delta t))|^2 \rangle$, where $\mathcal{F}$ indicates the Fourier transform, and $\mathbf{q} = (q_x, q_y)$ is the 2D wavevector in the Fourier space. If the system structure and dynamics are isotropic, an average can be performed over different orientations of $\mathbf{q}$, obtaining the azimuthally averaged image structure function $d(q, \Delta t)$, where $q = \sqrt{q_x^2 + q_y^2}$.

For each scattering wavevector q, the image structure function $d(q, \Delta t)$ is typically a monotonically increasing function of the delay time Δt, as shown in Figure 1b. The image structure function is given by

$$d(q, \Delta t) = A(q)[1 - f(q, \Delta t)] + B(q) \qquad (1)$$

where the term $A(q)$ is the static amplitude, and the term $B(q)$ accounts for the noise in the detection chain;[11] the function $f(q, \Delta t)$ is the real part of the intermediate scattering function, a quantity that is also probed in a DLS experiment for a fixed q set by the scattering angle $\theta = 2 \arcsin(q\lambda/\pi)$.[11,34] By fitting a suitable model to $d(q, \Delta t)$, one can thus extract $f(q, \Delta t)$, whose decay encodes the information on the sample dynamics at a length scale $2\pi/q$.[34]

In the simple case where the sample is a collection of monodisperse independent particles undergoing Brownian motion with a diffusion coefficient D, the intermediate scattering function is described by a single exponential decay $f(q, \Delta t) = \exp(-\Gamma(q)\Delta t)$, where the q-dependent relaxation rate $\Gamma(q)$ is given by $\Gamma(q) = Dq^2$.[34] For each q, fitting (eq 1) to $d(q, \Delta t)$, with $f(q, \Delta t) = \exp(-\Gamma(q)\Delta t)$, allows obtaining the relaxation rate $\Gamma(q)$. By fitting a quadratic model to the latter, one estimates the diffusion coefficient, which is linked to the particle hydrodynamic radius R_h via the Stokes−Einstein equation

$$D = \frac{k_B T}{6\pi\eta R_h} \qquad (2)$$

where $k_B = 1.38 \times 10^{-23}$ J/K is the Boltzmann constant, T is the sample absolute temperature, and η is the solvent viscosity. This way, one can estimate the typical size of the diffusing objects. If the solution contains particles of different sizes, the intermediate scattering function is given by the weighted sum of multiple exponential decays, each of which is associated with a different subpopulation of particles.[34] In this general case, similar to DLS, reconstructing the particle size distribution from the intermediate scattering function is a nontrivial task and, according to the complexity of the sample and to the signal-to-noise ratio, different approaches, like cumulant expansion[35] or inversion algorithms like CONTIN,[26] can be exploited.

■ RESULTS AND DISCUSSION

We performed DDM analysis on all samples, consisting of solutions of three different proteins (BSA, lysozyme, and pepsin) at different concentrations, as detailed in the Materials and Methods section. A comprehensive account of all the

collected data can be found in the Supporting Information. Representative image sequences are included in Supplementary Movies SM1, SM2, SM3, SM4, SM5, and SM6. In each movie, both raw and background-subtracted images are shown, while the corresponding intensity histograms before and after background subtraction are reported in Figures S1 and S2, respectively. We consider first the results obtained for the BSA solutions. Figure 2a shows a few representative intermediate
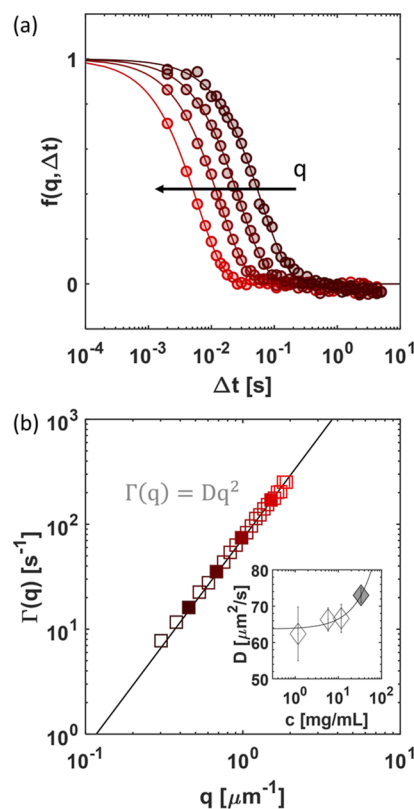

Figure 2. DDM analysis of diluted BSA solutions. (a) Representative intermediate scattering functions $f(q, \Delta t)$ at different wavevectors q for the BSA sample at concentration $c = 34 \pm 2$ mg/mL. The experimental data (circles) are fitted to a single exponential decay (solid lines). (b) Relaxation rate, $\Gamma(q)$ extracted from the fit. Solid symbols highlight the wavevectors q corresponding to the curves shown in panel (a). The solid line represents the quadratic fit to the data $\Gamma(q) = Dq^2$. The inset reports the values of diffusion coefficient D calculated from DDM analysis at different protein concentrations. The value corresponding to the sample at $c = 34 \pm 2$ mg/mL is highlighted in gray. The solid line represents a linear fit to the data according to eq 3.

scattering functions, $f(q, \Delta t)$, obtained at different wavevectors, q, for the most concentrated BSA solution ($c = 34 \pm 2$ mg/mL). As can be appreciated from the figure, the experimental data are well described by a single exponential decay. The q-dependence of the corresponding relaxation rate $\Gamma(q)$ obtained from the fit is reported in Figure 2b. A quadratic fit of $\Gamma(q) = Dq^2$ provides an estimated diffusion coefficient $D = (73 \pm 2)$ μm^2/s. The diffusion coefficients obtained with the same procedure for the BSA samples at lower concentrations (down to about 1.2 mg/mL) are plotted as a function of protein concentration in the inset of Figure 2b. The diffusion coefficient is observed to systematically increase with the protein concentration. Weak intermolecular interactions can indeed result in a dependency of the collective diffusion
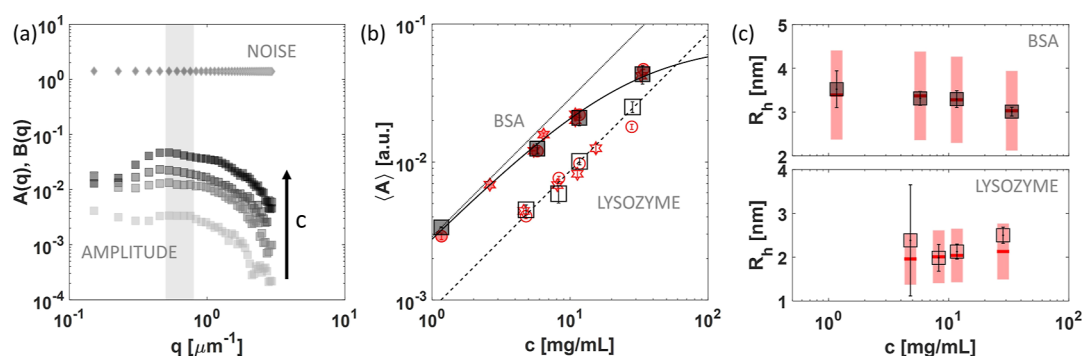
Figure 3. Signal amplitude and noise at different protein concentrations. (a) Signal amplitude $A(q)$ (squares) and noise term $B(q)$ (diamonds) measured for BSA solutions at different concentrations. (b) Scaling of the scattering intensity measured with DDM (black squares) and SLS (red symbols) as a function of protein concentration for BSA (solid symbols) and lysozyme (empty symbols) samples. DDM values are obtained as an average of $A(q)$ in the q range between 0.5 and 0.8 μm^{-1}, corresponding to the gray-shaded area in panel (a). The dashed and dotted lines correspond to linear scalings, while the solid black line is a fit to the BSA DDM data according to eq 5. Each SLS data set has been scaled with an arbitrary multiplicative constant. Red circles correspond to SLS measurements at λ = 405 nm and θ = 147°, whereas red stars correspond to measurements at λ = 532 nm and θ = 90°. (c) Hydrodynamic radii estimated with DDM (black squares) for single molecules of BSA (top) and lysozyme (bottom) at different concentrations. Values obtained from DLS are shown as red horizontal dashes, with vertical shaded bars representing the full width at half maximum of the size distributions.

coefficient D on the concentration c, which for semidiluted solutions reads

$$D = D_0(1 + k_D \cdot c) \tag{3}$$

where D_0 is the diffusion coefficient in the dilute limit and k_D is the so-called diffusion interaction parameter, which is expected to be positive in the case of repulsive interactions.[36] A linear fit to the data provides $D_0 = (64 \pm 4)$ $\mu m^2/s$ and $k_D = (4 \pm 1) \times 10^{-3}$ mL/mg, which is fully consistent with previously reported values for BSA under similar experimental conditions.[37]

To enable a direct comparison with the output of the DLS measurements, we calculated for each sample the corresponding hydrodynamic radius using the Stokes−Einstein relation (eq 2). The results are shown in Figure 3c. In the same figure, we also report the average hydrodynamic radius and the width of the number-weighted size distribution estimated for each sample with DLS (see Supporting Information Figure S1 and Supporting Information Table S2). As can be appreciated, the agreement between DDM and DLS results, as well as with literature reference values,[38] is very good. As a further consistency check, we independently estimate the diffusion interaction parameter k_D by fitting the model $R_h^{-1} = R_0^{-1}(1 + k_D \cdot c)$ to the DLS data. The fitting procedure gives $R_0 = (3.4 \pm 0.1)$ nm and an estimate of the diffusion interaction parameter $k_D = (4 \pm 1) \times 10^{-3}$ mL/mg, fully compatible with the value obtained with DDM.

Besides extracting the relaxation rate, the above-described procedure also enables estimation of the corresponding static amplitude $A(q)$, as well as the noise term $B(q)$, for each wavevector q.

In Figure 3a, we report the amplitude $A(q)$ and the noise baseline $B(q)$ measured for the BSA solutions at different concentrations. First of all, we note that the noise term $B(q)$ is nearly constant at all wavevectors and does not differ significantly between the samples. This is consistent with the fact that $B(q)$ mainly depends on the electronic noise of the sensor and on the shot noise,[11] which is expected to be constant as the imaging conditions and the camera settings are identical for all acquisitions. By contrast, the signal amplitude $A(q)$ systematically increases with the protein concentration. Indeed, for each given wavevector q, $A(q)$ is expected to be

directly proportional to the scattering intensity $I(q)$, $A(q) = T(q)I(q)$, where the proportionality term $T(q)$, often referred to as the optical transfer function, is an instrumental constant,[11] independent of the sample concentration. To investigate how the amplitude scales with the protein concentration, we consider the average value $\langle A \rangle$ over a defined range of q between 0.5 and 0.8 μm^{-1}, where $A(q)$ exhibits a very broad peak. The results are shown as solid symbols in Figure 3b. As can be appreciated from the figure, the amplitude displays a fairly linear dependence on the concentration for small c (dotted line), while a systematic deviation is observed at larger c. This behavior is compatible with the presence of repulsive interactions between the molecules, and it is described by the Debye−Zimm equation[39] which, for semidiluted solutions of particles much smaller than the wavelength of light, can be written as

$$\frac{K^* c}{\Delta R} = \frac{1}{M} + 2B_2 c \tag{4}$$

Here, ΔR is the Rayleigh ratio, K^* is an instrumental constant (which also incorporates the refractive index of the solvent and the refractive index increment dn/dc of the protein solution), M is the molecular mass, and B_2 is the second virial coefficient, which represents the first correction to the ideal gas equation of state due to interparticle interactions. For a given experimental geometry, the Rayleigh ratio is directly proportional to the scattering intensity I. We can thus rewrite eq 4 in terms of the average amplitude $\langle A \rangle$ as follows

$$\langle A \rangle = \frac{kc}{1 + c/c_0} \tag{5}$$

where k is a new constant accounting also for the effect of the optical transfer function, and $c_0 = (2MB_2)^{-1}$. By fitting eq 5 to our DDM data (and using M = 66.6 kDa), we obtain the following estimate for the second virial coefficient, $B_2 = (3 \pm 1) \times 10^{-4}$ mol·mL·g^{-2}. This value has the same order of magnitude but is significantly larger compared to most of the values reported in the literature for the same protein under similar conditions.[40] In order to confirm the validity of our findings, we performed static light scattering experiments on
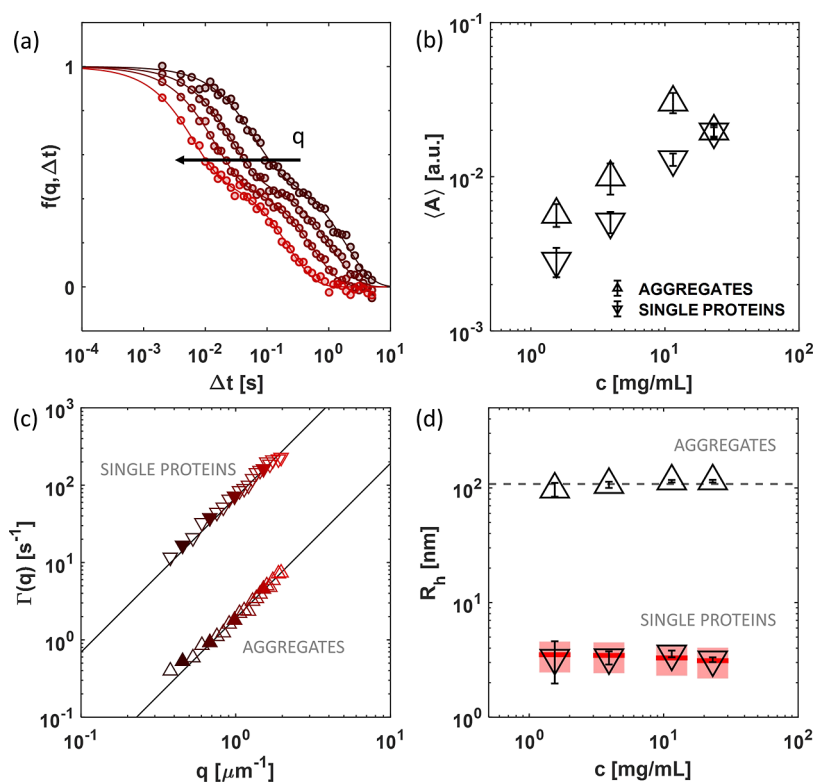
Figure 4. DDM analysis of diluted pepsin solutions. (a) Examples of intermediate scattering functions $f(q, \Delta t)$ at different wavevectors q for the pepsin sample at $c = 23 \pm 1$ mg/mL. Data clearly show a double decay due to the simultaneous presence of single and aggregated proteins. Experimental data (circles) are fitted with a double exponential (solid lines). (b) Scaling of the two amplitudes $\langle A_1 \rangle$ (single proteins) and $\langle A_2 \rangle$ (protein aggregates) with the protein concentration. (c) Relaxation rates Γ_1 and Γ_2 extracted from the fit at different q, linked to the motion of single proteins (down-pointing triangles) and protein aggregates (up-pointing triangles), respectively. Solid symbols highlight the selection of data points corresponding to the curves shown in (a). (d) Hydrodynamic radii of single proteins and aggregates, calculated from the diffusion coefficients obtained at different concentrations. The black dashed line represents the average size estimated for the protein aggregates, that is equal to about 108 nm. The red-shaded bars represent the full width at half maximum of the size distributions obtained from DLS, with average values indicated as red horizontal dashes.

the same proteins, obtaining the scattered intensity $I(c)$ at both 147° ($\lambda = 405$ nm) and 90° ($\lambda = 532$ nm) as a function of the concentration c. The results, scaled by a global multiplicative constant, are reported in Figure 3b as solid red circles and stars, respectively, and display an excellent agreement with the ones obtained with DDM.

Taken together, these results demonstrate that bright-field DDM, besides providing an accurate characterization of diluted and semidiluted protein solution dynamics, can also be used to characterize, at least in relative terms, the dependence of the scattering intensity on the concentration, gathering quantitative information on the intermolecular interactions.

A similar set of experiments was performed on a sequence of lysozyme solutions at concentrations ranging between 5 and 30 mg/mL. The obtained intermediate scattering functions are again fully compatible with a simple exponential decay, indicating a fairly monodisperse sample (Supporting Information). The estimates for the hydrodynamic radius obtained for each sample are reported in Figure 3c as empty symbols, where we can see that within the experimental errors, the estimated R_h values do not show any systematic dependence on the concentration. All values are in good agreement with both the literature[41] and DLS results (see Supporting Information Table S2). For lysozyme, the average amplitude $\langle A \rangle$ shown in Figure 3b (empty squares) displays a rather clean linear scaling with c

(dashed line), indicating a marginal effect of intermolecular interactions in the investigated concentration range. This result was also confirmed by independent static light-scattering measurements (empty red circles and stars).

While the results obtained for both BSA and lysozyme solutions are compatible with the behavior of a diluted suspension of identical particles, the pepsin solutions we investigated provide an example of a less ideal case. Indeed, despite filtration, DDM analysis revealed the presence of protein aggregates at all concentrations considered. The intermediate scattering functions are no longer described by a single exponential but display two well-distinct decays, as shown in Figure 4a for the highest concentration ($c = 23 \pm 1$ mg/mL). A good fit to the data is now obtained by adopting a double-exponential model of the form

$$f(q, \Delta t) = [1 - \alpha(q)e^{-\Gamma_1(q)\Delta t} - (1 - \alpha(q))e^{-\Gamma_2(q)\Delta t}].$$

This model corresponds to the simultaneous presence of two relaxation processes, which we attribute to two distinct families of diffusing particles. This can be confirmed by considering the q-dependence of the two relaxation rates, Γ_1 and Γ_2, extracted from the fit, as shown in Figure 4c. Both Γ_1 and Γ_2 display a rather clean $\sim q^2$ scaling. By fitting a quadratic function to the two rates, we determine the corresponding diffusion coefficients from which we recover the associated hydrodynamic radii reported in Figure 4d. Strikingly enough, the hydrodynamic radius $R_{h,1} = (3.2 \pm 0.2)$ nm corresponding to

the faster decay is in excellent agreement with the value $R_{h,DLS}$ = (3.11 ± 0.03) nm obtained from the DLS measurement, as well as with literature values for the monomeric protein under similar conditions.[42] This indicates that the "fast" contribution to the intermediate scattering function comes from the diffusion of monomeric, unaggregated proteins. On the other hand, the slower decay provides a hydrodynamic radius $R_{h,2}$ of about (115 ± 3) nm. This value is compatible with the size of the largest particle that can pass through the filter, whose nominal mesh size is about 220 nm. The amplitude $\langle A_1 \rangle = \langle \alpha \cdot A \rangle$ of the decay corresponding to single proteins and the amplitude $\langle A_2 \rangle = \langle (1 - \alpha) \cdot A \rangle$ obtained for the aggregates are both shown in Figure 4b, as down- and up-pointing triangles, respectively. As for lysozyme, we observe a fairly good linear scaling of $\langle A_1 \rangle$ with c for pepsin over the whole range of investigated concentrations.

It is worth noticing that while the amplitudes of the two contributions are somehow comparable ($1 \lesssim \langle A_2 \rangle / \langle A_1 \rangle \lesssim 2$, corresponding to $0.3 \lesssim \alpha \lesssim 0.5$), this is not true for the corresponding concentrations c_1 and c_2. Let M_1 and M_2 be the average molecular weights of the monomeric proteins and of the aggregates, respectively. Under the simplifying assumptions that both dn/dc and the density are the same for single and aggregated molecules, we get

$$\frac{c_2}{c_1} \simeq \frac{\langle A_2 \rangle / M_2}{\langle A_1 \rangle / M_1} \simeq \frac{\langle A_2 \rangle}{\langle A_1 \rangle} \left(\frac{R_{h,1}}{R_{h,2}} \right)^3 \simeq 8 \times 10^{-5}.$$

According to this estimate, the contribution of the aggregates to the total mass in the solution is very small (less than 0.01%), and we can safely assume that the concentration c_1 of the monomeric protein coincides with the total concentration c measured with the UV spectrophotometer. Remarkably, the presence of these aggregates is only barely visible in DLS measurements performed at large scattering angles (see Supporting Information Figure S1), which suggests how the access to the small scattering angles probed by DDM may be crucial to obtain a thorough sample characterization.

■ CONCLUSIONS

In this work, we have shown that DDM enables us to measure the size of proteins in solution in seconds using a bright-field microscope. The current detection limit in terms of concentration is about 1 mg/mL for BSA, only about a decade above the nominal sensitivity of typical commercial DLS instruments. The smallest detected molecule is lysozyme, with a hydrodynamic radius of about 2 nm. Importantly, these limits are by no means fundamental in nature as they are mainly determined by the intrinsic noise of the detector and by the size and number of acquired images. Indeed, we foresee that the adoption of new-generation, better-performing sensors, combined with the execution of more extended measurements, could significantly increase the sensitivity of the method as well as the accuracy in the determination of the particle size. In Supporting Information, we provide an in-depth examination of the instrumental factors (e.g., sample concentration, molecular weight, and camera specifications) that affect the signal-to-noise ratio for a protein sizing DDM experiment. From this, we derive an equation for the critical signal-to-noise ratio, the threshold below which DDM is unlikely to yield reliable results. This estimation serves a dual purpose: it can be used to predict whether the signal from a particular sample under the experimental conditions in place

will be strong enough for DDM analysis. Additionally, it can guide the optimization of the experimental protocol, ensuring that it is primed for detecting the sample of interest. While these results allow us to estimate the lower limit of detection (e.g., in terms of the minimum detectable concentration of a target molecule), an upper limit is imposed by the onset of multiple scattering, which breaks the simple linear relation between the amplitude of the concentration fluctuations in the sample and the optical signal in the images DDM relies on.[11] It is important to note, though, that this constraint mainly applies to extremely turbid samples. Under normal conditions,[27] DDM exhibits the capacity to effectively probe solutions with concentrations up to a thousand times higher than what conventional DLS can manage. Even within this effective range, it is crucial to keep in mind that interactions between the molecules in solution can affect their collective dynamics and lead to a collective diffusion coefficient D that deviates systematically from the one predicted by the Stokes−Einstein relation (eq 2),[34,36] as also shown in this study. As a consequence, DDM, like DLS, requires suitably diluted solutions to be used as a particle sizing tool. A common empirical approach to determine whether a given solution is diluted enough to enable reliable sizing consists of further diluting the solution (for example by a factor of 2), repeating the measurement on the diluted sample, and checking whether the diffusion coefficients obtained from the two samples are mutually consistent.[6] Alternatively, the diffusion coefficient in the dilute limit can be obtained by extrapolating to $c = 0$, the values obtained at different concentrations according to eq 3.

We have also shown that besides determining the relaxation dynamics, with DDM it is also possible to obtain quantitative information on the dependence of the scattered intensity on the concentration and hence on intermolecular interactions, an application that could be pushed further by calibrating the microscope with small colloidal particles to determine the transfer function $T(q)$.

In each experiment presented in this work, the volume probed in a single measurement was as small as $\simeq$20 nL. This indicates that our approach, combined with suitably designed sample cells, allows the investigation of extremely small sample volumes.

Notably, by probing much smaller wavevectors (typically in the range $[0.1, 10]$ μm^{-1}) compared to fixed 90° angle DLS ($q_{DLS} \simeq 17$ μm^{-1}, assuming $\lambda = 532$ nm), DDM enables characterizing the dynamics of rapidly diffusing particles with relatively relaxed requirements in terms of the sampling frequency. For example, the light scattered at 90° by an aqueous solution of 2 nm particles fluctuates with a characteristic time of about 30 μs. The same solution probed at $q \simeq 1$ μm^{-1} displays fluctuations with a $\simeq 9$ ms lifetime, which can be easily captured with a standard scientific camera.

In this study, we focused on a few relatively simple representative examples where the particle size distribution is strongly peaked around either one or two well-defined values. However, the range of applicability of the method is much wider. As already mentioned, the whole paraphernalia of DLS can be directly exploited to analyze and interpret DDM data: cumulant expansion to evaluate sample polydispersity,[22,24,35] inversion schemes to estimate the particle size distribution, like CONTIN,[26] to mention a few.

■ ASSOCIATED CONTENT

Ⓢ Supporting Information

The Supporting Information is available free of charge at https://pubs.acs.org/doi/10.1021/acs.macromol.3c00782.

Estimation of the critical signal-to-noise ratio and the detection limit; concentration values measured with UV spectrophotometry; DLS results; examples of typical image intensity histograms; and representative intermediate scattering functions $f(q, \Delta t)$, amplitude $A(q)$, noise term $B(q)$, and relaxation rate $\Gamma(q)$ for each sample (PDF)

Representative movie of BSA sample at the lowest concentration (AVI)

Representative movie of BSA sample at the highest concentration (AVI)

Representative movie of lysozyme sample at the lowest concentration (AVI)

Representative movie of lysozyme sample at the highest concentration (AVI)

Representative movie of pepsin sample at the lowest concentration (AVI)

Representative movie of pepsin sample at the highest concentration (AVI)

■ AUTHOR INFORMATION

Corresponding Authors

Roberto Cerbino − *Faculty of Physics, University of Vienna, Wien, Vienna 1090, Austria;* ⓞ orcid.org/0000-0003-0434-7741; Email: roberto.cerbino@univie.ac.at

Fabio Giavazzi − *Dipartimento di Biotecnologie Mediche e Medicina Traslazionale, Università degli Studi di Milano, Segrate (MI) 20054, Italy;* ⓞ orcid.org/0000-0003-4930-0592; Email: fabio.giavazzi@unimi.it

Authors

Chiara Guidolin − *Dipartimento di Biotecnologie Mediche e Medicina Traslazionale, Università degli Studi di Milano, Segrate (MI) 20054, Italy*

Christopher Heim − *NanoTemper Technologies GmbH, Munich 81369, Germany*

Nathan B. P. Adams − *NanoTemper Technologies GmbH, Munich 81369, Germany*

Philipp Baaske − *NanoTemper Technologies GmbH, Munich 81369, Germany*

Valeria Rondelli − *Dipartimento di Biotecnologie Mediche e Medicina Traslazionale, Università degli Studi di Milano, Segrate (MI) 20054, Italy;* ⓞ orcid.org/0000-0001-8409-9025

Complete contact information is available at:
https://pubs.acs.org/10.1021/acs.macromol.3c00782

Notes

The authors declare no competing financial interest.

■ ACKNOWLEDGMENTS

■ REFERENCES

(1) Pecora, R. d. Doppler shifts in light scattering from pure liquids and polymer solutions. *J. Chem. Phys.* **1964**, *40*, 1604−1614.

(2) Debye, P. Spectral width of the critical opalescence due to concentration fluctuations. *Phys. Rev. Lett.* **1965**, *14*, 783−784.

(3) Einstein, A. *Investigations on the Theory of the Brownian Movement*; Courier Corporation, 1956.

(4) Dubin, S. B.; Lunacek, J. H.; Benedek, G. B. Observation of the spectrum of light scattered by solutions of biological macromolecules. *Proc. Natl. Acad. Sci. U.S.A.* **1967**, *57*, 1164−1171.

(5) Foord, R.; Jakeman, E.; Oliver, C.; Pike, E.; Blagrove, R.; Wood, E.; Peacocke, A. Determination of diffusion coefficients of haemocyanin at low concentration by intensity fluctuation spectroscopy of scattered laser light. *Nature* **1970**, *227*, 242−245.

(6) Stetefeld, J.; McKenna, S. A.; Patel, T. R. Dynamic light scattering: a practical guide and applications in biomedical sciences. *Biophys. Rev.* **2016**, *8*, 409−427.

(7) Hulst, H. C.; van de Hulst, H. C. *Light Scattering by Small Particles*; Courier Corporation, 1981.

(8) Pusey, P. Suppression of multiple scattering by photon cross-correlation techniques. *Curr. Opin. Colloid Interface Sci.* **1999**, *4*, 177−185.

(9) Pine, D. J.; Weitz, D. A.; Chaikin, P. M.; Herbolzheimer, E. Diffusing wave spectroscopy. *Phys. Rev. Lett.* **1988**, *60*, 1134−1137.

(10) Cerbino, R.; Trappe, V. Differential dynamic microscopy: probing wave vector dependent dynamics with a microscope. *Phys. Rev. Lett.* **2008**, *100*, 188102.

(11) Giavazzi, F.; Brogioli, D.; Trappe, V.; Bellini, T.; Cerbino, R. Scattering information obtained by optical microscopy: differential dynamic microscopy and beyond. *Phys. Rev. E: Stat., Nonlinear, Soft Matter Phys.* **2009**, *80*, 031403.

(12) Bayles, A. V.; Squires, T. M.; Helgeson, M. E. Dark-field differential dynamic microscopy. *Soft Matter* **2016**, *12*, 2440−2452.

(13) Lu, P. J.; Giavazzi, F.; Angelini, T. E.; Zaccarelli, E.; Jargstorff, F.; Schofield, A. B.; Wilking, J. N.; Romanowsky, M. B.; Weitz, D. A.; Cerbino, R. Characterizing concentrated, multiply scattering, and actively driven fluorescent systems with confocal differential dynamic microscopy. *Phys. Rev. Lett.* **2012**, *108*, 218103.

(14) Brizioli, M.; Sentjabrskaja, T.; Egelhaaf, S. U.; Laurati, M.; Cerbino, R.; Giavazzi, F. Reciprocal space study of Brownian yet non-Gaussian diffusion of small tracers in a hard-sphere glass. *Front. Phys.* **2022**, *10*, 408.

(15) Bayles, A. V.; Squires, T. M.; Helgeson, M. E. Probe microrheology without particle tracking by differential dynamic microscopy. *Rheol. Acta* **2017**, *56*, 863−869.

(16) Edera, P.; Bergamini, D.; Trappe, V.; Giavazzi, F.; Cerbino, R. Differential dynamic microscopy microrheology of soft materials: A tracking-free determination of the frequency-dependent loss and storage moduli. *Phys. Rev. Mater.* **2017**, *1*, 073804.

(17) Cerbino, R.; Giavazzi, F.; Helgeson, M. E. Differential dynamic microscopy for the characterization of polymer systems. *J. Polym. Sci.* **2022**, *60*, 1079−1089.

(18) Wilson, L. G.; Martinez, V. A.; Schwarz-Linek, J.; Tailleur, J.; Bryant, G.; Pusey, P.; Poon, W. C. Differential dynamic microscopy of bacterial motility. *Phys. Rev. Lett.* **2011**, *106*, 018101.

(19) Martinez, V. A.; Besseling, R.; Croze, O. A.; Tailleur, J.; Reufer, M.; Schwarz-Linek, J.; Wilson, L. G.; Bees, M. A.; Poon, W. C. Differential dynamic microscopy: A high-throughput method for characterizing the motility of microorganisms. *Biophys. J.* **2012**, *103*, 1637−1647.

(20) Giavazzi, F.; Malinverno, C.; Scita, G.; Cerbino, R. Tracking-free determination of single-cell displacements and division rates in confluent monolayers. *Front. Phys.* **2018**, *6*, 120.

(21) Latreille, P.-L.; Rabanel, J.-M.; Le Goas, M.; Salimi, S.; Arlt, J.; Patten, S. A.; Ramassamy, C.; Hildgen, P.; Martinez, V. A.; Banquy, X. In Situ Characterization of the Protein Corona of Nanoparticles In Vitro and In Vivo. *Adv. Mater.* **2022**, *34*, 2203354.

(22) Safari, M. S.; Vorontsova, M. A.; Poling-Skutvik, R.; Vekilov, P. G.; Conrad, J. C. Differential dynamic microscopy of weakly

scattering and polydisperse protein-rich clusters. *Phys. Rev. E: Stat., Nonlinear, Soft Matter Phys.* **2015**, *92*, 042712.

(23) Giavazzi, F.; Crotti, S.; Speciale, A.; Serra, F.; Zanchetta, G.; Trappe, V.; Buscaglia, M.; Bellini, T.; Cerbino, R. Viscoelasticity of nematic liquid crystals at a glance. *Soft Matter* **2014**, *10*, 3938−3949.

(24) Giavazzi, F.; Haro-Pérez, C.; Cerbino, R. Simultaneous characterization of rotational and translational diffusion of optically anisotropic particles by optical microscopy. *J. Phys.: Condens. Matter* **2016**, *28*, 195201.

(25) Cerbino, R.; Piotti, D.; Buscaglia, M.; Giavazzi, F. Dark field differential dynamic microscopy enables accurate characterization of the roto-translational dynamics of bacteria and colloidal clusters. *J. Phys.: Condens. Matter* **2018**, *30*, 025901.

(26) Provencher, S. W. CONTIN: a general purpose constrained regularization program for inverting noisy linear algebraic and integral equations. *Comput. Phys. Commun.* **1982**, *27*, 229−242.

(27) Nixon-Luke, R.; Arlt, J.; Poon, W. C.; Bryant, G.; Martinez, V. A. Probing the dynamics of turbid colloidal suspensions using differential dynamic microscopy. *Soft Matter* **2022**, *18*, 1858−1867.

(28) Jepson, A.; Martinez, V. A.; Schwarz-Linek, J.; Morozov, A.; Poon, W. C. Enhanced diffusion of nonswimmers in a three-dimensional bath of motile bacteria. *Phys. Rev. E: Stat., Nonlinear, Soft Matter Phys.* **2013**, *88*, 041002.

(29) Drechsler, M.; Giavazzi, F.; Cerbino, R.; Palacios, I. M. Active diffusion and advection in Drosophila oocytes result from the interplay of actin and microtubules. *Nat. Commun.* **2017**, *8*, 1520.

(30) Giavazzi, F.; Savorana, G.; Vailati, A.; Cerbino, R. Structure and dynamics of concentration fluctuations in a non-equilibrium dense colloidal suspension. *Soft Matter* **2016**, *12*, 6588−6600.

(31) Lago, P.; Rovati, L.; Cantù, L.; Corti, M. A quasielastic light scattering detector for chromatographic analysis. *Rev. Sci. Instrum.* **1993**, *64*, 1797−1802.

(32) Germain, D.; Leocmach, M.; Gibaud, T. Differential dynamic microscopy to characterize Brownian motion and bacteria motility. *Am. J. Phys.* **2016**, *84*, 202−210.

(33) Verwei, H. N.; Lee, G.; Leech, G.; Petitjean, I. I.; Koenderink, G. H.; Robertson-Anderson, R. M.; McGorty, R. J. Quantifying cytoskeleton dynamics using differential dynamic microscopy. *J. Visualized Exp.* **2022**, *184*, No. e63931.

(34) Berne, B. J.; Pecora, R. *Dynamic Light Scattering: With Applications to Chemistry, Biology, and Physics*; Courier Corporation, 2000.

(35) Frisken, B. J. Revisiting the method of cumulants for the analysis of dynamic light-scattering data. *Appl. Opt.* **2001**, *40*, 4087−4091.

(36) Harding, S. E.; Johnson, P. The concentration-dependence of macromolecular parameters. *Biochem. J.* **1985**, *231*, 543−547.

(37) Larsen, H. A.; Atkins, W. M.; Nath, A. Probing interactions of therapeutic antibodies with serum via second virial coefficient measurements. *Biophys. J.* **2021**, *120*, 4067−4078.

(38) Jachimska, B.; Wasilewska, M.; Adamczyk, Z. Characterization of globular protein solutions by dynamic light scattering, electrophoretic mobility, and viscosity measurements. *Langmuir* **2008**, *24*, 6866−6872.

(39) Zimm, B. H. The scattering of light and the radial distribution function of high polymer solutions. *J. Chem. Phys.* **1948**, *16*, 1093−1099.

(40) Ma, Y.; Acosta, D. M.; Whitney, J. R.; Podgornik, R.; Steinmetz, N. F.; French, R. H.; Parsegian, V. A. Determination of the second virial coefficient of bovine serum albumin under varying pH and ionic strength by composition-gradient multi-angle static light scattering. *J. Biol. Phys.* **2015**, *41*, 85−97.

(41) Wilkins, D. K.; Grimshaw, S. B.; Receveur, V.; Dobson, C. M.; Jones, J. A.; Smith, L. J. Hydrodynamic radii of native and denatured proteins measured by pulse field gradient NMR techniques. *Biochemistry* **1999**, *38*, 16424−16431.

(42) Gtari, W.; Bey, H.; Aschi, A.; Bitri, L.; Othman, T. Impact of macromolecular crowding on structure and properties of pepsin and trypsin. *Mater. Sci. Eng. C* **2017**, *72*, 98−105.

▢ Recommended by ACS

Differential Dynamic Microscopy: Diffusion Measurements Where You Want Them

Xujun Zhang, Paul S. Russo, *et al.*

DECEMBER 17, 2023

MACROMOLECULES   READ ↗

Real-Time Optical Tracking of Protein Corona Formation on Single Nanoparticles in Serum

Mathias Dolci, Peter Zijlstra, *et al.*

OCTOBER 06, 2023

ACS NANO   READ ↗

Rapid Estimation of Size-Based Heterogeneity in Monoclonal Antibodies by Machine Learning-Enhanced Dynamic Light Scattering

Anuj Shrivastava, Anurag S. Rathore, *et al.*

MAY 18, 2023

ANALYTICAL CHEMISTRY   READ ↗

Analysis of Silicon Quantum Dots and Serum Proteins Interactions Using Asymmetrical Flow Field-Flow Fractionation

Usharani Nagarajan, Françoise M. Winnik, *et al.*

MAY 24, 2023

LANGMUIR   READ ↗

Get More Suggestions >